The terminal solid solubility of hydrogen in irradiated Zircaloy-2 and microscopic modeling of hydride behavior

K. Une [a,*], S. Ishimoto [a], Y. Etoh [a], K. Ito [b], K. Ogata [c], T. Baba [c], K. Kamimura [c], Y. Kobayashi [d]

[a] Nippon Nuclear Fuel Development, Co., Ltd., 2163 Narita-cho, Oarai-machi, Ibaraki-ken 311-1313, Japan
[b] Global Nuclear Fuel Japan Co., Ltd., 3-1 Uchikawa 2-chome, Yokosuka-shi, Kanagawa-ken 239-0836, Japan
[c] Japan Nuclear Energy Safety Organization, 3-17-1 Toranomon, Minato-ku, Tokyo 105-0001, Japan
[d] M.O.X. Corporation, 1828-520 Hirasu-cho, Mito-shi, Ibaraki-ken 310-0853, Japan

ABSTRACT

Differential scanning calorimetry (DSC) has been applied to elucidate the terminal solid solubility (TSS) of hydrogen in Zircaloy-2 cladding tubes and spacer bands irradiated in commercial BWRs. While recovery of irradiation defects during the first heating stage of as-irradiated specimens made the DSC peak of hydride dissolution dull or broader, no significant difference was detected in the TSS between unirradiated and irradiated Zircaloy-2, irrespective of fast neutron fluence. The effect of post-irradiation annealing on TSS was also examined. The results suggest almost no interaction between irradiation defects and dissolved hydrogen or hydrides at temperatures around 300 °C. Using the present TSS data and reported hydrogen- and hydride-related properties, a microscopic analysis code HYMAC for analyzing hydride behavior in cladding tube with textured grains was constructed. Stress-induced preferential precipitation and dissolution of hydrides were reproduced by adopting a TSS sub-model in which the solubilities decrease in proportion to stress normal to the habit plane in grains and to grain faces. Analyzed results by the code were consistent with typical experimental results of hydride behavior.

© 2009 Elsevier B.V. All rights reserved.

1. Introduction

Hydride-related embrittlement of fuel cladding and structural material made of Zr alloys is one of the most important issues limiting light water reactor fuel performance at high burnup; for example, the outside-in type cracking in high burnup BWR cladding arising at power ramp tests [1]. When considering hydride behavior in Zr alloys, the terminal solid solubility (TSS) of hydrogen for hydride dissolution (TSSD) and hydride precipitation (TSSP) is a prime factor, and for further detailed quantitative analyses, a mechanistic and microscopic model containing TSS data is needed. There is only limited TSS data for irradiated Zr alloys, compared to the data for unirradiated materials. Within the authors' knowledge, there are two papers [2,3] regarding TSS measurements for irradiated materials, both carried out by means of differential scanning calorimetry (DSC). Though these studies recognized the increase of hydrogen solubility in irradiated Zircaloys, the increments differed considerably in each. As a mechanism for the increase of solubility, trapping of dissolved hydrogen by irradiation damage was suggested. In contrast, assuming the existence of some interactions between microscopic hydrides and irradiation defects [4], TSSD of irradiated material would become lower than that of unirradiated material.

In this work, DSC measurements were made for the purpose of confirming whether any meaningful changes in TSS data, or significant trapping effects, are apparent in Zircaloy-2 irradiated in commercial BWRs. Though part of the data has been already reported as a short communication [5], a full set of the data and detailed discussion are presented in this paper. Special attention is paid to the DSC responses, i.e. the competing phenomena of inherent endothermic reaction due to hydride dissolution and exothermic reaction due to recovery of irradiation defects. Moreover, using the present TSS data and reported hydrogen- and hydride-related properties, a microscopic model of hydride behavior was constructed for the purpose of analyzing hydride-related phenomena of stress reorientation of hydride, thermal diffusion of hydrogen, and delayed hydride cracking (DHC). In the model, the concept of stress-induced decrease of TSS plays an important role.

2. Experimental

2.1. Materials

Irradiated Zircaloy-2 specimens approximately 4 mm square (30–80 mg) were prepared from cladding tubes and spacer bands, which had been irradiated during 3 and 5 cycles in commercial BWRs. The alloy compositions of Zircaloy-2 in wt% were 1.30–1.37 Sn, 0.16–0.18 Fe, 0.10–0.11 Cr, 0.06–0.07 Ni and 0.11–0.13

O, with the balance Zr. Oxide films on the outer surface and Zr liner of the cladding tube were removed in advance before cutting DSC specimens. Hydrogen concentrations were analyzed after DSC measurements using the hot vacuum extraction method with an accuracy of ±3%. Fast neutron fluence ($E > 1$ MeV) and hydrogen concentration of the specimens were 7.9–12.9 × 10^{25} n/m^2 and 21–194 ppm for the cladding tubes, and 5.4–8.5 × 10^{25} n/m^2 and 166–373 ppm for the spacer bands (see Table 1). The cladding specimens were irradiated in a temperature range of 288–340 °C along the tube wall, and the spacer bands were at a constant temperature of 288 °C. Metallographs of 3 and 5 cycle irradiated specimens are given in Fig. 1, showing typical hydride morphology. Note that the photos of the cladding specimens (Fig. 1(a) and (b)) were taken before removing the inner Zr liner and outer surface regions, while the photo of the spacer band (Fig. 1(c)) was taken after removing both two surfaces. In contrast to the fairly uniform distribution of hyde strings seen in the spacer specimen, nonuniform hydride distribution is distinguished in the cladding specimens, especially in the Zircaloy-2 region close to Zr liner, which arises from a lower hydrogen solubility in pure Zr compared to that in Zircaloy-2 [6,7].

In addition to measurements of the irradiated Zircaloy-2 specimens, data for unirradiated specimens were obtained as a reference, using archived cladding and spacer band materials. These were hydrogenated in advance by (1) corrosion reactions in water vapor at 400–450 °C for 24 h or in LiOH solution at 290–320 °C for 16–24 h, and (2) by a gaseous hydrogenation in a He/2%H$_2$ mixed gas at 485–515 °C for 5 min. The hydrogenation treatment of hydrides was followed by an annealing treatment at 480 °C for 4 h in vacuum. The obtained hydrogen concentration ranged from 40 to 358 ppm for the cladding specimens and 31–410 ppm for the spacer specimens. The details of the hydrogenation procedure were described previously [6].

2.2. Differential scanning calorimetry

The TSSD and TSSP temperatures of the specimens were measured using the differential scanning calorimetry (DSC) technique. Details of the DSC instrument (Netzsch DSC-404) used were given previously [8]. The DSC measurements were carried out in purified Ar at a flow rate of 20 cm^3/min in the same manner as the previous studies for unirradiated Zircaloy-2 and high Fe Zircaloy [6], and unalloyed ziroconium [7]. In all the measurements, a sample was first heated from 50 °C to the planned terminal temperatures, followed by cooling down to 120 °C, with a hold-time of 5 min at

the maximum temperature. A heat up and cool down rate of 10 °C min^{-1} was adopted. This rate was chosen because a fast rate provides higher DSC sensitivity. For all the unirradiated and irradiated specimens, three measuring runs were performed. The analysis of DSC peaks resulting from hydride dissolution during heat up and hydride precipitation during cool down followed the procedure previously recorded [6].

3. TSS results and discussion

3.1. DSC response of irradiated Zircaloy-2

Typical examples of the DSC curves together with their time derivation (DDSC) for as-irradiated specimens containing 26 (DS35-34, cladding) and 182 ppm hydrogen (DSS1-1, spacer), obtained during the heat up and cool down stages of the first and third runs, are shown in Figs. 2 and 3, respectively. The maximum terminal temperatures were 310 °C for the former and 540 °C for the latter. In the cladding specimen, the terminal temperature was determined as low as possible, to minimize any annealing of irradiation damage.

In the heat up DSC curve of the low hydrogen concentration (26 ppm) specimen in Fig. 2, small endothermic peaks are narrowly detected around 230–250 °C. TSS temperatures have been defined as the maximum slope in the DSC curve, i.e. the peak observed in DDSC curves [6,7]. This peak, corresponding to complete hydride dissolution via endothermic reaction, becomes clearer as measurement runs are repeated. This evolution may arise from a change of hydride morphology, or hydride agglomeration, as opposed to annealing of irradiation defects, because the terminal temperature and holding time were 310 °C and only 5 min. As detailed later, exothermic reactions resulting from the recovery of irradiation defects occur when temperatures are around 280 °C, just corresponding to the irradiation temperature in BWR. In the cool down DSC curves, a clear DDSC peak corresponding to the precipitation of hydrides was not detected, except for a tiny peak at 164 °C in the third run curve (Fig. 2(d)). The reason for the steep change of DSC base line at about 160 °C was caused by small deviations from the constant cooling rate of 10 °C min^{-1}. Consequently, the reliability of TSSP temperature measurements for the low hydrogen specimens seems to be lower than other specimens with higher hydrogen contents.

For the case of higher hydrogen concentration (182 ppm) specimen in Fig. 3, a broad DDSC peak was observed during the first

Table 1
DSC specimens and TSSD/TSSP temperatures for three runs.

Specimen no.	Hydrogen content (ppm)	Neutron fluence -(x10^{25} n/m^2)	TSSD (°C)			TSSP (°C)			Terminal temperature (°C)	Post-irradiation Annealing
			Run 1	Run2	Run 3	Run 1	Run 2	Run3		
DS01-1 (cladding)	24	8.1	235.8	225.1	228.7	166.8	167.1	165.7	350, 400, 400	As-irradiated
DS01-2 (cladding)	21	8.1	256.1	220.9	225.1	–	–	–	310, 310, 310	As-irradiated
DS35-12 (cladding)	26	7.9	254.4	248.7	247.4	164.9	152.0	153.3	350, 400, 400	As-irradiated
DS35-34 (cladding)	26	7.9	255.6	241.1	240.9	–	–	163.7	310, 310, 310	As-irradiated
DS69-1 (cladding)	194	12.9	398.8	397.4	399.0	332.6	323.8	320.8	540, 540, 540	As-irradiated
DS69-2 (cladding)	144	12.9	385.8	370.0	370.9	291.1	289.6	289.4	540, 540, 540	As-irradiated
DS69-3 (cladding)	154	12.9	365.3	378.6	380.2	299.1	306.5	310.5	450, 450, 450	[*]1
DS69-6 (cladding)	140	12.9	356.7	365.3	369.6	281.2	281.2	282.1	450, 450, 450	360 °C × 3 h
DS69-7 (cladding)	156	12.9	389.2	371.0	369.5	287.9	287.8	287.9	540, 540, 540	As-irradiated
DSS1-1 (spacer)	182	5.4	380.1	385.9	386.4	307.5	305.0	304.9	540, 540, 540	As-irradiated
DSS1-3 (spacer)	166	5.4	375.1	382.1	379.9	298.0	298.3	298.6	450, 450, 450	340 °C × 3 h
DSS2-1 (spacer)	373	8.5	448.8	453.3	452.0	384.1	383.1	383.3	540, 540, 540	As-irradiated
DSS2-2 (spacer)	341	8.5	450.2	454.5	456.5	383.2	382.8	383.8	540, 540, 540	340 °C × 3 h
DSS2-3 (spacer)	372	8.5	451.0	457.7	458.0	389.0	389.1	389.3	540, 540, 540	As-irradiated

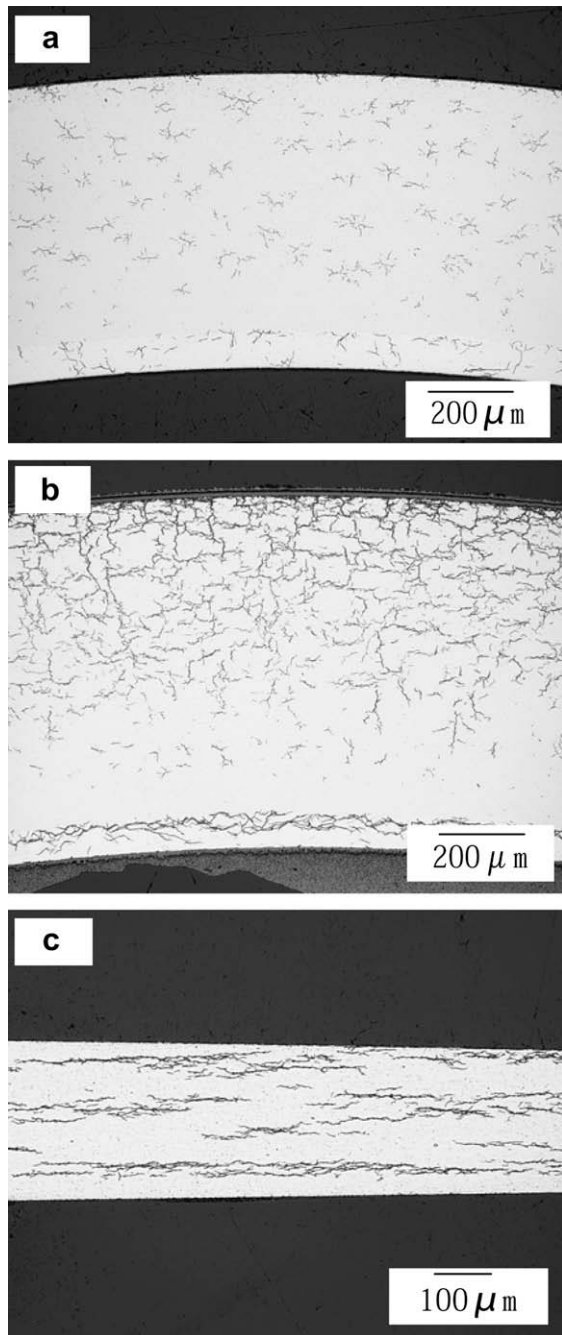[*] 1 before 1st run: 360 °C × 3h; before 2nd run: 485 °C × 2h; before 3rd run: 600 °C × 1 h.

Fig. 1. Metallographs of irradiated Zircaloy-2. (a) 3 cycle irradiated cladding (DS35), (b) 5 cycle irradiated cladding (DS69), (c) 3 cycle irradiated spacer band (DSS1).

heating stage. In the second and third heating stages, sharper DDSC peaks corresponding to hydride dissolution are distinguished at temperatures not so different from that seen in the first run. Looking closely at the DDSC curves, endothermic TSSD peak width tends to become sharper with repeated measurement runs, especially from the first to the second run. Moreover, it is noteworthy that in the heating curve of the first DSC run, some exothermic contribution obviously adds to the original endothermic reaction of hydride dissolution for temperatures above 300 °C. The effect becomes remarkable above 350–360 °C, and appears to override the original endothermic TSSD peak in the first heating stage. As before, this irreversible exothermic reaction is caused by the recovery of irradiation defects. The sharpening of the DSC and DDSC peaks during the second and third heating stages was brought about by

the heat experience of 540 °C at least once or two times, and almost no change in TSSD temperature was observed from the second to third runs.

Fig. 4(a) and (b) show the heating and cooling DSC responses for the post-irradiation annealed specimen of 166 ppm hydrogen concentration (DSS1-3) during the first run. The annealing condition was 340 °C for 3 h. Compared to the corresponding DSC response of the as-irradiated specimen of 182 ppm in Fig. 3 (DSS1-1), no exothermic effect was obvious up to the annealing temperature of 340 °C. Another important point is that there is a clear inflection point in the DSC curve, i.e. a clear peak in DDSC. This TSSD temperature of 375 °C is reasonably accepted to be somewhat lower than that (380 °C) for the as-irradiated specimen of 182 ppm. The annealing treatment of 340 °C for 3 h made the mixed endothermic and exothermic reactions clear.

Fig. 5(a) and (b) show at what temperature irradiation defects start to recover for the as-irradiated (DSS1-1) and post-irradiation annealed (DSS1-3) spacer specimens, respectively. The difference (ΔDSC) in heating DSC signal between the third and first runs, and the third and second runs, is plotted against temperature; ΔDSC value was normalized as zero at 150 °C. Since the DSC response of the third run can be regarded as most stabilized condition for irradiation defects among the three runs, ΔDSC would correspond conceptually to recovery rate of irradiation defects. It is obvious that for the as-irradiated specimen the recovery during the first run starts at the temperature of 280 °C, which corresponds to the irradiation temperature, and the recovery rate increases rapidly with temperature up to 450 °C. In the second heating run, a slight recovery is apparent above 480 °C even after being subjected previously to 540 °C. In the case of the post-irradiation annealed specimen, the recovery starts around 340 °C during the first run, coinciding with the post-irradiation annealing temperature. No recovery is detectable during the second run.

Consequently, special attention on the recovery phenomenon of irradiation damage is needed whenever evaluation of TSSD temperatures is undertaken using thermal analysis, such as DSC, DTA and TMA.

3.2. TSS of irradiated Zircaloy-2

Table 1 summarizes TSSD and TSSP temperatures for the irradiated specimens, together with hydrogen content, fast neutron fluence, post-irradiation annealing condition and DSC terminal temperature. The data for unirradiated specimens were not tabled. Some of the as-irradiated specimens were subjected to post-irradiation annealing treatment at 340–360 °C for 3 h before DSC measurements, in order to examine the influence of damage recovery on DSC response and TSS temperature.

The TSSD data for the unirradiated specimens were compared with four published data sets for Zircaloy-2 and Zircaloy-4 (Fig. 6), including our previous data for Zircaloy-2 material with a different fabrication history [6]. In the figure, three of the four published data sets plotted were obtained by the DSC technique, the exception being Kearns' data [9] which was evaluated by an equilibrium method. Two of the data sets, by McMinn et al. [2] and Vizcaino et al. [3], were obtained as reference data for comparison with irradiated specimen data. The present TSSD data for unirradiated Zircaloy-2 are reasonably consistent with the 4 published data sets.

The Arrhenius plots of the solvi of TSSD and TSSP for the irradiated Zircaloy-2 obtained in the first run are shown in Fig. 7. In the figure, the data of the unirradiated specimens and their regression line are also given. When comparing the TSSD data of the irradiated specimens with the unirradiated ones, a reasonable coincidence between them is obvious, though some deviation is seen for the low hydrogen content (21–26 ppm) specimens. This is
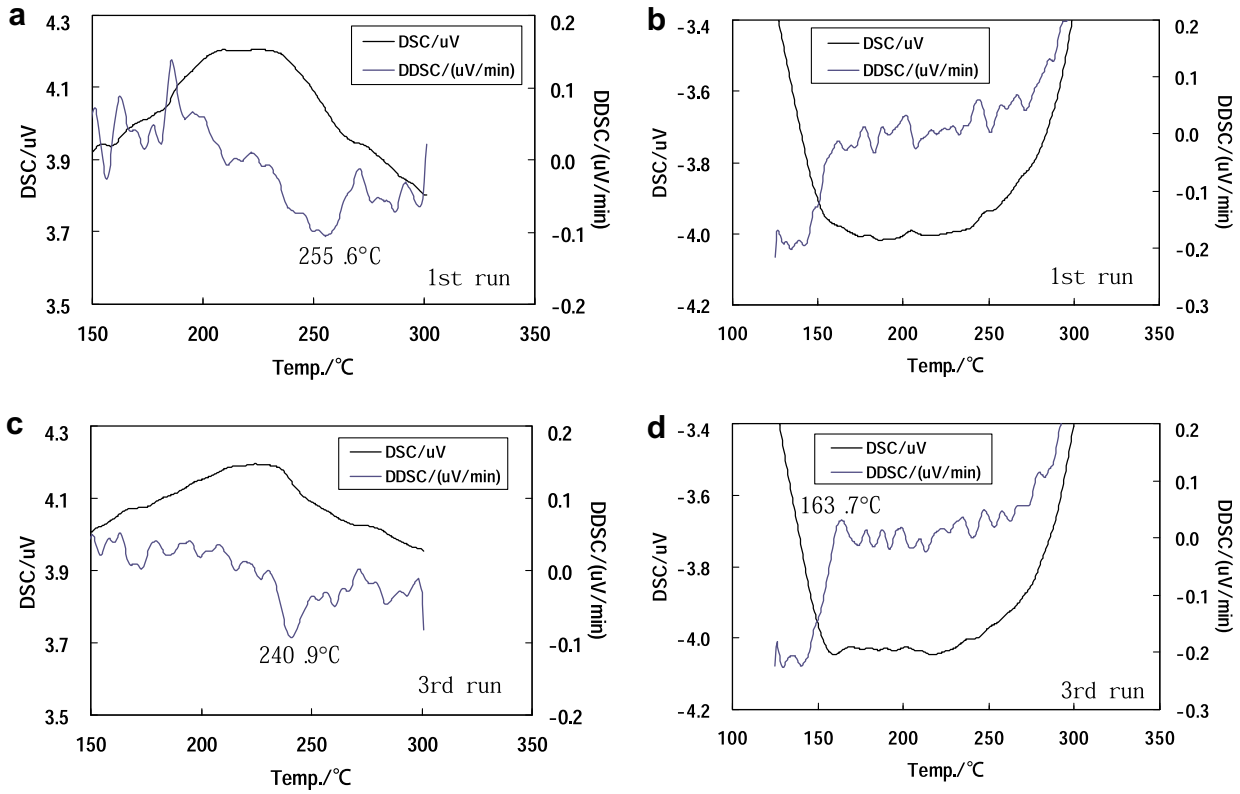
Fig. 2. DSC responses of the first and third runs during heating and cooling stages for the 3 cycle irradiated cladding (DS35-34). (a) and (c) are the heat up responses, (b) and (d) are the cool down responses.
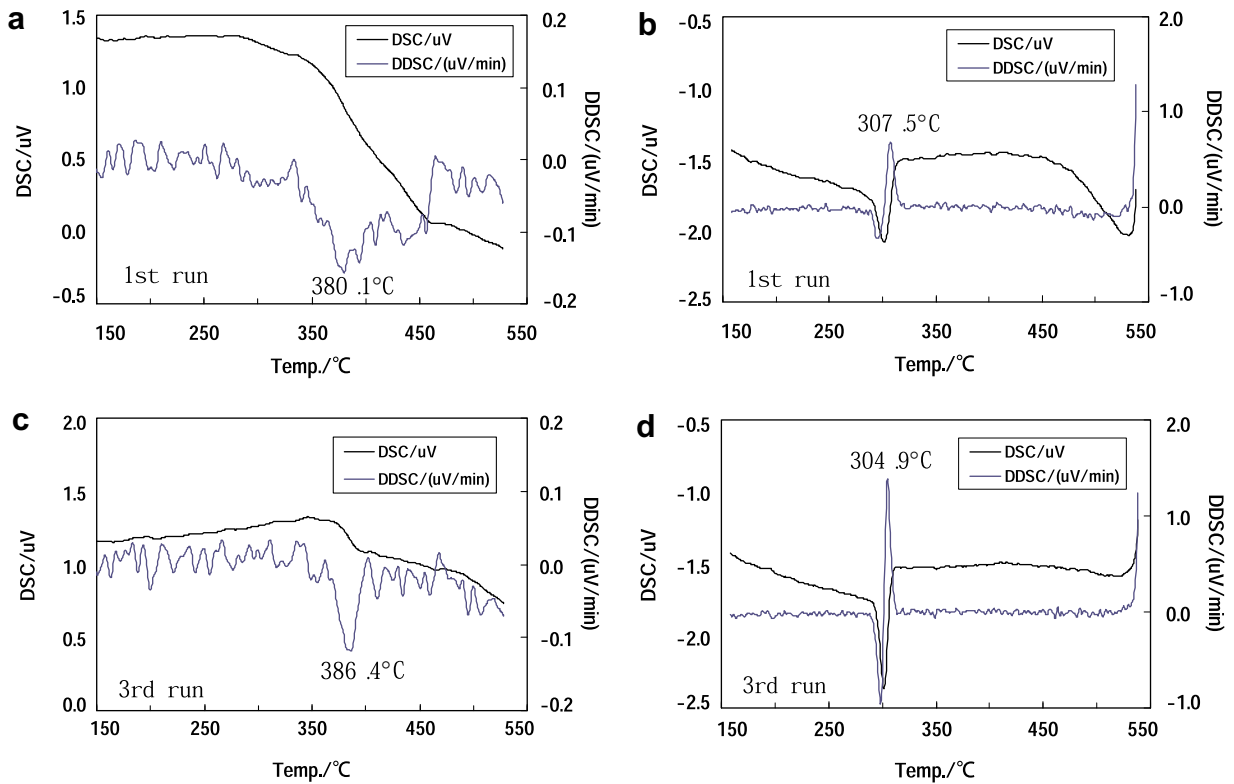

Fig. 3. DSC responses of the first and third runs during heating and cooling stages for the 3 cycle irradiated spacer band (DSS1-1). (a) and (c) are the heat up responses, (b) and (d) are the cool down responses.
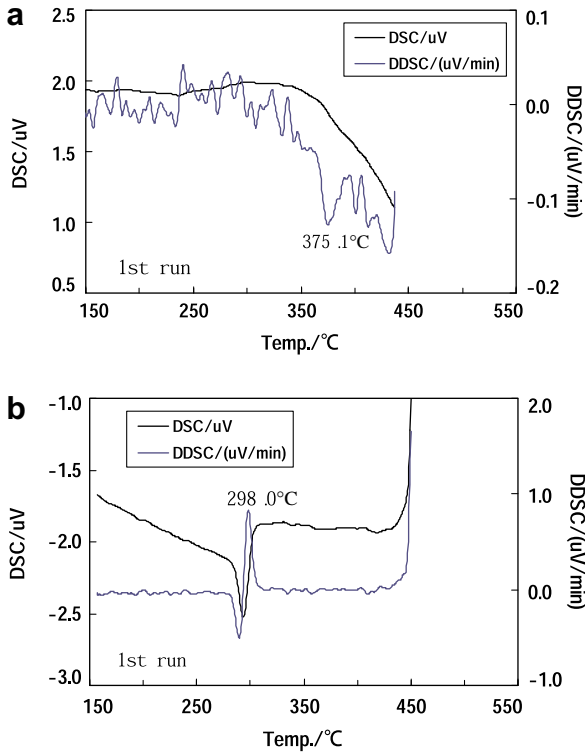
Fig. 4. DSC responses of the first run during (a) heating and (b) cool down stages for the 3 cycle irradiated spacer band after post-irradiation annealing at 340 °C for 3 h (DSS1-3).
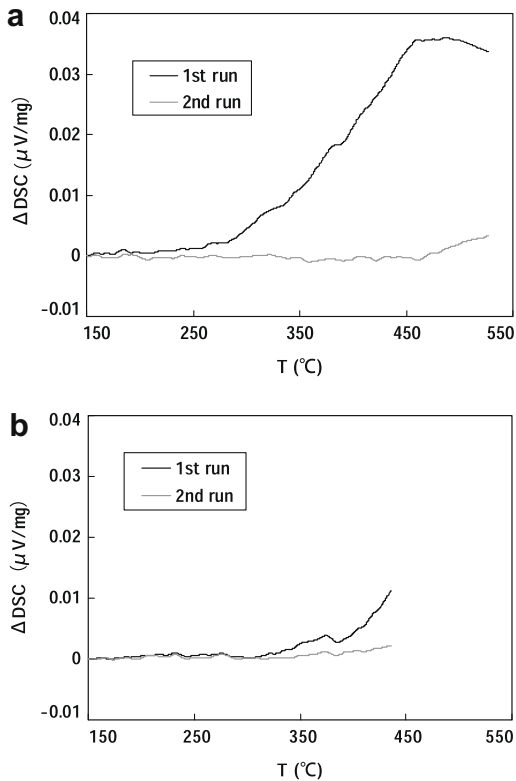

Fig. 5. Difference in heatup DSC signal, ΔDSC, between the third and first runs, and the third and second runs, for the (a) as-irradiated specimen (DSS1-1), and (b) post-irradiation annealed specimen (DSS1-3). ΔDSC was normalized to zero at 150 °C.
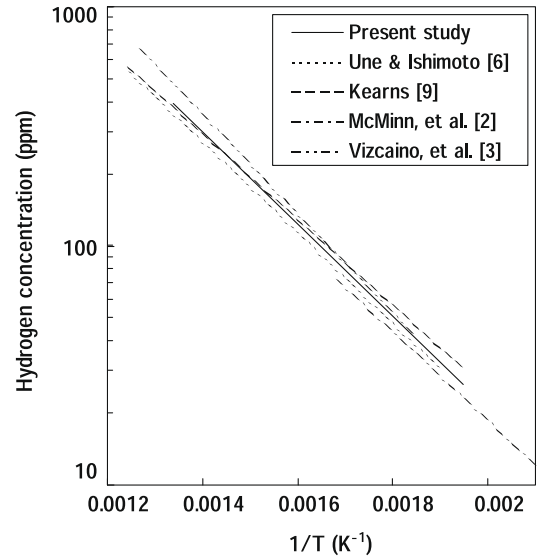

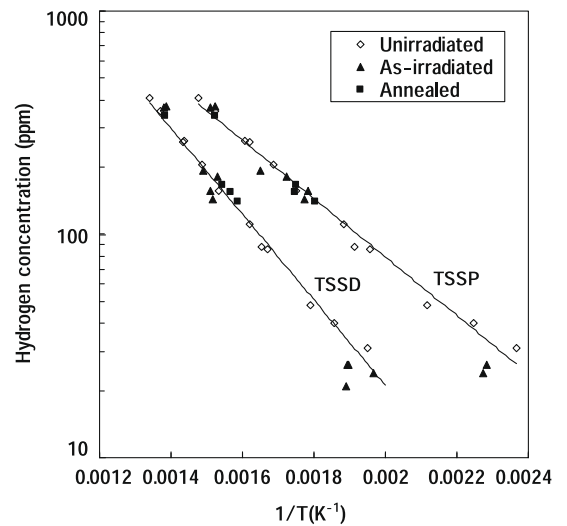**Fig. 6.** Comparison of TSSD solvus for unirradiated Zircaloys.

Fig. 7. Solvi of TSSD and TSSP for irradiated Zircaloy-2, together with the corresponding unirradiated Zircaloy-2. The regression lines are derived from the data of the unirradiated Zircaloy-2.

mainly attributable to the unstable hydride morphology, as discussed earlier, because their TSSD temperatures are certainly lower than the irradiation temperature of 280 °C at which substantial defect recovery starts. In fact, the second and third run temperatures came close to the regression line of the unirradiated materials. The TSSD data for the high hydrogen content (140–373 ppm) specimens have almost the same deviation from the regression line as the unirradiated specimens, and there is no significant difference between the as-irradiated and post-irradiation annealed specimens. As described in the previous Section 3.1, the recovery process starts at the irradiation temperature for the as-irradiated specimens and at the post-irradiation annealing temperature for the annealed specimens, and it becomes remarkable above 350–360 °C. TSSD temperatures for the high hydrogen content specimens appear in this defect recovery temperature range. When comparing the data of the cladding and spacer band specimens of 140–182 ppm hydrogen with different fast neutron fluences (cladding: 12.9×10^{25} n/m²; spacer band: 5.4×10^{25} n/m²), no

difference is obvious, indicating no effect of fast neutron fluence on TSS.

TSSP temperatures derived in the cool down stage were, of course, obtained after subjecting the specimens to the DSC terminal temperature at least once. With the exception of the less reliable low hydrogen content (24 and 26 ppm) specimen data which resulted from poor DSC responses, TSSP data obtained in the first run are well expressed by the regression line for the unirradiated specimens, similar to the result observed for the TSSD data. As seen in DSC responses during the cool down stage of Figs. 2 and 3, clear and sharp TSSP peaks were detected, which was brought about by an annihilation of large amounts of irradiation defects through subjection of the specimen to 450 °C or 540 °C. Nevertheless, the TSSP temperatures observed during the first run for the high hydrogen specimens did not change significantly even in the second or third runs. For the low hydrogen content specimens, although the second and third run TSSP data shifted slightly toward the regression line, relatively large deviations still remained. However, when considering the combined reliability of the present DSC measurement and hydrogen analysis using small specimens of about 30–80 mg, there is no concrete basis to propose a new TSSP regression line for the irradiated Zircaloy-2. Consequently, best-fit equations for the TSSD and TSSP solvi of irradiated, as well as unirradiated, Zircaloy-2 are given by Eqs. (1) and (2) for a hydrogen concentration of 21–373 ppm:

$$C_{TSSD} \text{ (ppm)} = 1.43 \times 10^5 \exp(-36,686/RT), \tag{1}$$

$$C_{TSSP} \text{ (ppm)} = 3.27 \times 10^4 \exp(-25,042/RT) \tag{2}$$

where R is the gas constant (8.314 J K^{-1} mol^{-1}) and T the temperature in K.

This result, that there is no significant difference in both TSSD and TSSP solvi between irradiated and unirradiated Zircaloy-2, contrasts that of two other studies [2,3] which reported that the solubilities in Zircaloys obtained by the same DSC technique as the present study increase more or less by neutron irradiation. McMinn et al. [2] obtained TSSD and TSSP solvi of Zircaloy-2 and Zircaloy-4 with 15–75 ppm hydrogen content, which had been irradiated at 250–300 °C in a test reactor to fast neutron fluences of 0.6–10 × 10^{25} n/m^2. The specimen conditions were both as-irradiated and hydrided by diffusion annealing at 260 °C after irradiation. Unirradiated specimens were homogenized at 400 °C for 48 h after hydrogenation treatment. Their TSSD and TSSP were higher than those for the corresponding unirradiated specimens by about 5–10 ppm for TSSD and 10–20 ppm for TSSP with no dependences of hydrogen concentration and fast neutron fluence. After annealing at 500 °C, full recovery of these irradiation effects was observed. From the reported annealing characteristics of irradiation damage, the possibility of some interaction or trapping of dissolved hydrogen by irradiation damage, such as <a>-type dislocations, was suggested. However, the difference in hydride morphology between the unirradiated and irradiated specimens with different temperature histories, may affect TSS temperatures, as possibly seen in the present low hydrogen specimens.

Another TSSD study was carried out by Vizcaino et al. [3], who used irradiated Zircaloy-4 specimens prepared from pressure tubes of a HWPR. The irradiation temperature was in a range of 263–298 °C, and hydrogen concentrations absorbed during reactor operation were about 150–380 ppm. Significant TSSD increases of 100 ppm and more were detected, and the effects of measuring run and high temperature annealing on TSSD examined. From the fact that TSSD temperature difference between the irradiated and unirradiated specimens did not disappear entirely even after repeated annealing at high temperatures of 508–611 °C, Vizcaino et al. suggested that the increases of TSSD were attributable to strong trapping (of dissolved hydrogen) effects by irradiation
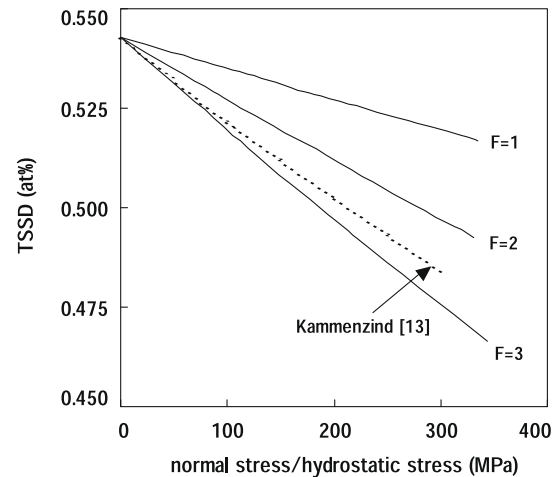

Fig. 8. Stress dependence of TSSD used in the model. F is the stress effect coefficient.

defects of <c>-type dislocations as well as <a>-type dislocations. However, there may exist two important inconsistencies in the TSSD results employed. If large amounts of dissolved hydrogen of more than 100 ppm are trapped by irradiation defects, no hydride precipitation should be observed in metallographs, SEM or TEM micrographs for irradiated Zircaloys containing a level of about 100 ppm. Unfortunately, metallographs of the specimens were not reported. However, hydride precipitates are commonly observed even in low hydrogen content (20–30 ppm) specimens, as observed in this study and shown in Fig. 1. Another point is that Vizcaino et al. did not consider the effects of exothermic reactions caused by the recovery of irradiation defects on the DSC response, which appear significantly above irradiation temperatures. Indeed, in their DSC curve for the as-irradiated specimen of 179 ppm hydrogen content reported in their subsequent paper [10], an exothermic response can be seen from about 270 °C. From this DSC response, Vizcaino et al. derived a TSSD temperature of 289 °C. However, almost constant TSSD temperatures of 250–300 °C, irrespective of hydrogen concentrations of 150–380 ppm (Fig. 8 in Ref. [3]) and which corresponds to the irradiation temperatures used by Vizcaino et al., may result from the complicated DSC response in irradiated materials.

4. Microscopic modeling of hydride behavior

4.1. Model description

An analysis code HYMAC (Hydride Microscopic Analysis Code) for the purpose of analyzing hydrogen and hydride behavior in the cladding tube was constructed, using the present TSS data and reported hydrogen- and hydride-related properties. The code consists of two programs of making zirconium grain structure with texture, and analyzing hydrogen diffusion and hydride behavior of precipitation and dissolution.

4.1.1. Hydrogen diffusion model

In this model, hydrogen diffusion driven by gradients of hydrogen concentration, temperature and stress as expressed by Eq. (3) was analyzed in two dimensional space of circumferential and radial directions of the cladding tube.

$$J_H = -\frac{D_H}{\Omega_{Zr}} \cdot \left\{ \nabla C_H - \frac{C_H}{R \cdot T} \cdot V_H^* \cdot \nabla \sigma_h + \frac{C_H}{R \cdot T^2} \cdot Q_H^* \cdot \nabla T \right\}, \tag{3}$$

where J_H is the hydrogen flux, C_H the hydrogen concentration in solution, D_H the diffusion coefficient of hydrogen, Ω_{Zr} the atomic volume of zirconium, V_H^* the volume of transport of hydrogen, Q_H^* the heat of transport of hydrogen, σ_h the hydrostatic stress, and R and T are the gas constant ($8.314 \, J \, K^{-1} \, mol^{-1}$) and temperature in K.

The diffusional space was sub-divided into square meshes, and is overlaid by Zr grains of hexagonal structure with texture (*c*-axis direction). Each square of the mesh is classified into grain or grain boundary mesh, and texture data analyzed by X-ray diffractometry are assigned for each grain mesh. Consequently, each grain mesh has its own *c*-axis direction. In this space, hydrogen diffusion, hydride precipitation/growth and dissolution, and delayed hydride cracking kinetics are analyzed by the difference method.

4.1.2. TSS model and local stress analysis

Stress-induced preferential precipitation and growth of hydrides at local sites may be explained by local hydrogen solubility, depending on local stress. That is, hydrides begin to precipitate preferentially at local sites of grains and grain boundaries where the stresses normal to the habit plane ((0001) basal plane of Zr grain) or normal to the grain faces are larger than other sites. This concept, that the solubilities decrease with tensile stress, comes from previous electron backscattering diffraction pattern (EBSP) examinations [11,12], focusing on crystallographic orientation of the Zr grain and hydride. Importantly, it was determined that the habit plane did not change with tensile stress, and that the local sites for hydride precipitation change preferentially under tensile stress.

In this model, the stress dependence of TSSD and TSSP adopted is described by Eq. (4):

$$TSSD \text{ or } TSSP = TSSD_O \text{ or } TSSP_O \times \exp\left(-\frac{\Delta W_{additional} + \sigma \cdot F}{R \cdot T}\right) \quad (4)$$

$$\Delta W_{additional} = (a \times f_{random}^1 + b_G \times f_{random}^2 + b_B \times f_{random}^3) \cdot F,$$

where $TSSD_O$, and $TSSP_O$ are the terminal solid solubilities at stress free condition, σ is the principal stress (boundary tensile stress or crack hydrostatic stress), F is the stress effect coefficient, $\Delta W_{additional}$ is the statistical additional stress factor, and a, b_G and b_B represent the fluctuation coefficient of each mesh (1 MPa fixed), the grain mesh coefficient and the grain boundary mesh coefficient, respectively. f_{random} is the random function. Fig. 8 shows the stress dependence of TSSD in the model with $F = 1$, 2 and 3, together with experimental data by Kammenzind et al. [13].

In the biaxial stress condition of $\sigma_l = 1/2\sigma_t$ (σ_l and σ_t are the axial and circumferential stress), the stress normal to the habit plane in the radial-circumferential plane of the cladding tube is expressed by:

$$\sigma_n(\phi, \alpha) = \sin^2\phi \cdot (1.0 - 0.5 \times \sin^2\alpha) \cdot \sigma_t, \quad (5)$$

where Φ is the angle between the *c*-axis and cladding radial direction in the radial-circumferential plane, and α is the angle between the *c*-axis and cladding circumferential direction in the axial-circumferential plane. Consequently, at the situation of $\Phi = 90°$ and $\alpha = 0°$, σ_n becomes maximum. These two angles are given to each mesh from the texture data obtained by X-ray diffractometry.

The grain face stress normal to grain boundaries may be given by an expression similar to that of Eq. (5), if the (0001) basal plane is replaced with a local grain face of an equivalent grain sphere. In this situation, the segment between grain center and grain face corresponds hypothetically to the *c*-axis of Zr single crystal, and Φ and α are the corresponding angles of the segment. Considering the geometrical configurations of any grain faces (or grain lines) sectioned by the observation plane, the value of α would depend on grain size, as expressed by:

$$\alpha(G_{observed} < G_{average}) = 90 - 90 \times \sqrt{\frac{G_{observed}}{G_{average}}} \quad (6)$$

$$\alpha(G_{observed} \geqslant G_{average}) = 0,$$

where $G_{observed}$ and $G_{average}$ are the observed and average grain sizes in the observation plane.

The model can be used to analyze the kinetics of delayed hydride cracking (DHC), in which hydride at the tip of radial crack can only grow straight. The crack propagation rate is assumed to be equal to the hydride growth rate, and not controlled by any fracture characteristics of hydrides. The model adopts an analytical solution for hydrostatic stress distribution [14] resulting from crack propagation, taking the stress in the plastic strain region adjacent to the crack tip to be approximated by $\sigma_y \times F$, where σ_y is the yield stress of material and F ranges between 2 and 3. This stress concentration decreases rapidly with distance from the crack tip. Principal or effective stress working on each mesh, which directly determines the hydrogen solubilities, is defined by either the boundary normal stress or the crack hydrostatic stress, depending on which is of larger value; near the crack tip hydrostatic stress is the principle stress, while elsewhere the boundary normal stress is the principal stress.

Finally, TSSD and TSSP in each mesh can be calculated by Eq. (4). Fig. 9 shows an example of TSSD distribution in each mesh when a circumferential stress of 300 MPa is applied to Zircaloy-2 tubing with a Zr liner at a uniform temperature of 300 °C. The lower TSSD in the Zr liner is due to the fact that pure Zr has a lower TSSD than Zircaloy-2 [7]. Near the DHC crack tip, TSSD drops steeply as a result of the very large hydrostatic stress. Naturally each grain boundary mesh has different TSSD values, and grain meshes belonging to one grain with the same *c*-axis orientation have slightly different TSSD values because of the effect of the addition stress factor, $\Delta W_{additional}$ of Eq. (4). This TSSD distribution controls hydride growth and shrinkage, while a similar distribution of TSSP controls hydride precipitation.

4.1.3. Hydride precipitation, growth and shrinkage model

Supersaturated hydrogen in solution beyond TSSP starts to precipitate into nuclei of hydride. Within the model, only one hydride
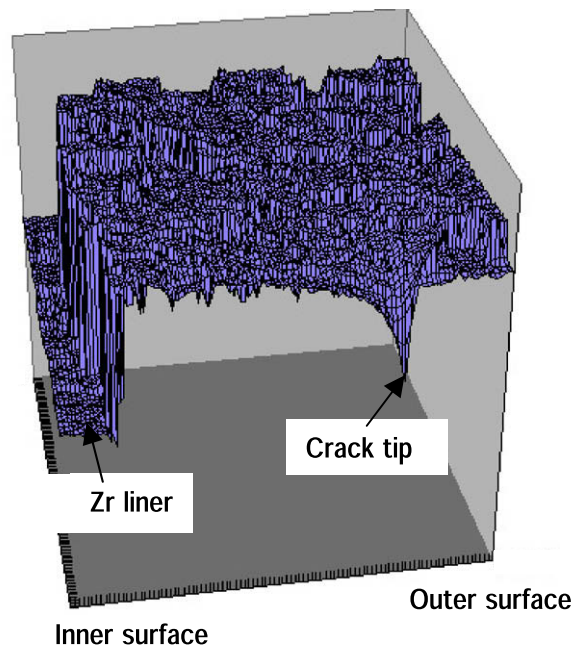

Fig. 9. Calculated TSSD distribution in the cladding with a radial crack under isothermal conditions (300 °C) and circumferential stress of 300 MPa.

nucleus is allowed to precipitate in each mesh, and the probability of hydride precipitation, Q, in a given mesh of hydrogen concentration C may be expressed by:

$$Q = f_{time} \times R_{loc} \times \left(\frac{Max(C - TSSP)_t}{(C_{ave} - TSSP_{min})_{ini}} \right)^{f1} \times Q_0 \qquad (7)$$

$$Q_0 = \left(\frac{(C - TSSP)_t}{Max(C - TSSP)_t} \right)^{f2},$$

where f_{time} is a time control factor, R_{loc} is a mesh region control factor, $Max(C–TSSP)_t$ is the maximum supersaturation of the system at a given time, $(C_{ave}–TSSP_{min})_{ini}$ is the maximum supersaturation of the system initially, $(C–TSSP)_t$ is the supersaturation of every mesh at a given time, and f^1 and f^2 are supersaturation distribution coefficients.

This type of formulation is aimed at reproducing a precipitation probability according to local TSSP distribution and random dispersion of hydrides in the system. When hydride precipitation starts, Q decreases exponentially because the value of $Max(C–TSSP)_t$ decreases with time. Number densities of hydride nuclei and their distribution are tuned deliberately by f_{time} and R_{area} by comparing with experimental results. Superiority of precipitation sites in grains or grain boundaries is controlled by local TSSP in each mesh through a balance of b_G and b_B in Eq. (4).

The flow diagram of the hydriding process is given in Fig. 10, including hydrogen diffusion, hydride precipitation, and hydride growth and shrinkage. In the mesh where hydride precipitation arises, the hydrogen concentration close to hydride becomes TSSD instantaneously, and the average hydrogen concentration becomes lower than those of the surrounding meshes. Sufficient hydrogen diffusion starts to occur along the gradient of hydrogen concentration toward the hydrided mesh and thus the precipitated hydride can grow further. As the hydride level in a mesh reaches a saturation level (hydride-saturated mesh), the hydride extends to adjacent meshes, according to the following rules:

- Hydrides cannot have branch, i.e. hydride string can only grow at the front edges.
- Hydride precipitated in grains can grow and develop along the habit plane. When a growing hydride reaches the grain bound-

aries, a new hydride not belonging to the parent hydride is recognized at the boundaries.
- Hydride precipitated at the grain boundaries can grow along the boundaries or can develop to neighboring grain meshes, depending on the local TSSD of the surrounding meshes.

When the hydrogen concentration in a mesh becomes lower than TSSD, the hydride will shrink only at the front edges of hydrides. If this occurs in a hydride-saturated mesh, it becomes an unsaturated hydrided mesh, with the hydride continuing to shrink until it finally disappears.

4.2. Model application

Thermo-chemical and thermo-physical properties related to hydrogen and hydride, and mechanical properties of Zircaloy-2 used in model applications are listed in Table 2. All the analyses presented here were carried out in a system of 100×100 mesh, and the saturation level of hydrided mesh was 0.1.

4.2.1. Precipitation and growth rates of hydride

The precipitation probability of hydrides was adjusted by tuning f_{time} and R_{area} of Eq. (7), and the number density and morphology of hydrides were compared with the metallographs of hydrides obtained in the previous DSC examination for unirradiated Zircaloy-2 sheet [6]. The combined rates of precipitation and growth from a condition of hydrogen supersaturated were also calculated. The calculation conditions are as follows: initial hydrogen concentration, 1.8 at.% (204 ppm); solution temperature, 350 °C; cooling rate, 0.167 °C/s.

Fig. 11(a) shows calculated transients of average concentrations of dissolved hydrogen and hydride in the system when the temperature is decreased from 350 to 250 °C without any external stress. A comparison between calculated and observed hydride morphology with the same magnification is given in Fig. 11(b) and (c). Simulated grain size is about $15\times$ larger than that of the real grain size of about 3–4 μm, largely because of the limited mesh number used. Number density of hydrides is about 300–350 n/mm² for both the experimental and calculated results. In the calculated hydride morphology of Fig. 11(b), many hydrides are grown within grains with circumferential orientation, similar to the observed situation. This originates from the texture of Zircaloy-2; the direction of in-grain hydrides is parallel to the basal plane of (0001). Around 340 °C, hydrides start to precipitate, and grow rapidly in a short time. Average rate of hydride precipitation and growth in this initial stage is 0.008 at.%/s (0.9 ppm/s), which is in good accordance with the result obtained by the previous DSC measurement using Zircaloy-2 with 1.8 at.% hydrogen [6]. The hydride precipitation DSC response obtained during the cooling stage exhibited a sharp transient in a lapse of about 90 s, corresponding to average precipitation rates of 0.006–0.009 at.%/s (0.7–1.0 ppm/s).
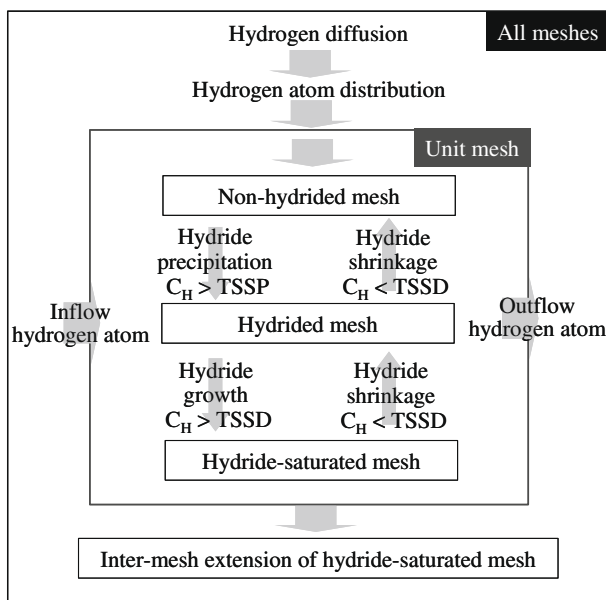

Fig. 10. Flow diagram of the hydriding process in the model.

Table 2
Parameters used in the model.

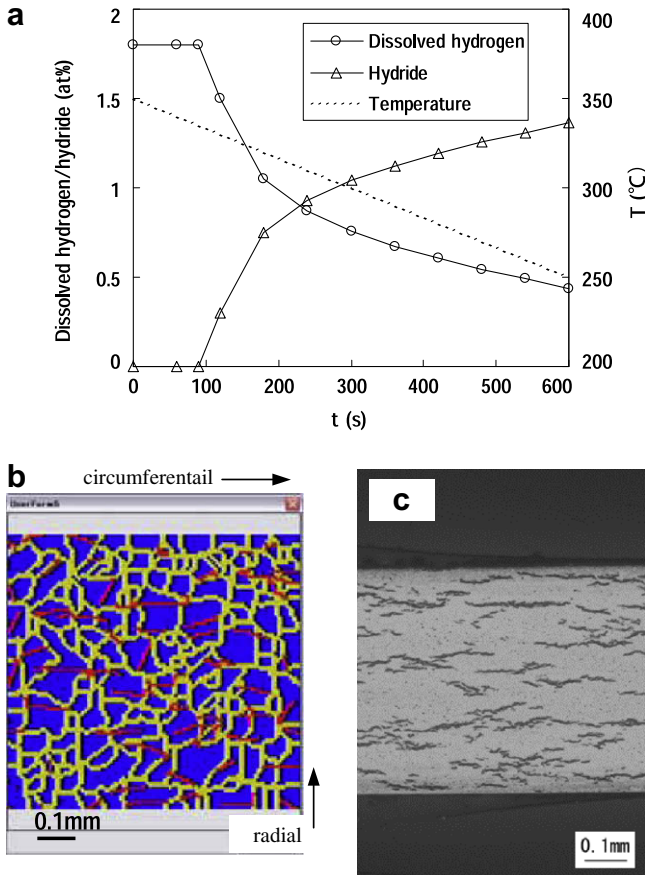| Parameter	Numerical value	References
TSSD (Zircaloy-2)	$1.43 \times 10^5 \exp(-36{,}686/RT)$ ppm	Present study
TSSP (Zircaloy-2)	$3.27 \times 10^4 \exp(-25{,}042/RT)$ ppm	Present study
TSSD (Zr)	$1.41 \times 10^5 \exp(-38{,}104/RT)$ ppm	[7]
TSSP (Zr)	$3.39 \times 10^4 \exp(-27{,}291/RT)$ ppm	[7]
Ω_{Zr}	2.3×10^{-29} m³/atom	[14]
D_H	$2.17 \times 10^{-7} \exp(-35{,}100/RT)$ m²/s	[21]
Q_H^*	25,100 J/mol	[22]
V_H^*	7.0×10^{-7} m³/mol	[23]
σ_y (irradiated)	$888 - 0.668 \times T(K)$ MPa	[24]
σ_y (unirradiated)	$1{,}102 - 0.913 \times T(K)$ MPa	[24]

Fig. 11. Hydride precipitation transients (a) and hydride morphology (b) calculated under the condition of Zircaloy-2 with 1.8 at.% hydrogen from solution temperature of 350 to 250 °C (red line = hydride; yellow line = grain boundary); metallograph of Zircaloy-2 cooled under the corresponding condition (c) (For interpretation of the references to colour in this figure legend, the reader is referred to the web version of this article.)

Fig. 12. Calculated stress reorientation of hydrides and hydride morphplogies when Zircaloy-2 cladding with 2 at.% hydrogen was cooled from 400 to 300 °C at a rate of 0.67 °C/s.

4.2.2. Stress reorientation of hydride

There are many published reports regarding stress reorientation of hydrides in Zr alloys under various test conditions. Generally, it is a phenomenon recognized as being important at stresses above 50–100 MPa [15–17]. Stress reorientation of hydrides was simulated by cooling Zircaloy-2 with 2 at.% (223 ppm) hydrogen in solution from 400 to 300 °C at a rate of 0.67 °C/s, and then maintaining 300 °C. When tensile stress is applied in the circumferential direction of the cladding tube, precipitation and growth sites of hydrides are expected to change to preferable grains with basal plane inclined to tensile direction and to preferable grain boundaries facing tensile direction.

The results of this simulation are shown in Fig. 12, together with the hydride morphologies at σ_t = 0 and 300 MPa. The F_n value is defined by the fraction of hydrides within ±45° of the radial direction. It increases even at low stress of 50 MPa, and shows a clear stress dependence, which is roughly consistent with experimental data [16,17]. As predicted, at σ_t = 300 MPa hydrides precipitate and grow preferentially in circumferentially textured grains and grain boundaries facing the tensile direction.

4.2.3. DHC kinetics

The propagation rate of delayed hydride cracking (DHC) in Zircaloy-2 tube, 0.71 mm thick with Zr liner of 0.09 mm, was analyzed under isothermal conditions. Initial crack length and hydrogen content were assumed to be 0.13 mm and 2 at.% (223 ppm), and tensile stress was 200 MPa. The above conditions
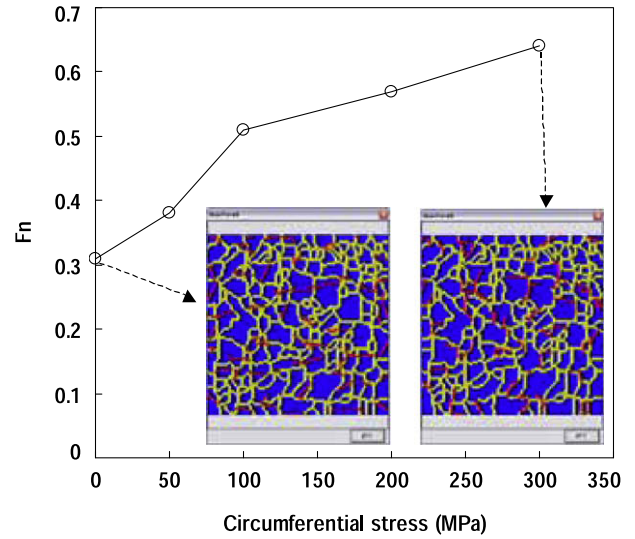
follow the experimental conditions of Sakamoto and Nakatsuka [18].

Fig. 13 shows a comparison of the calculated DHC rates with those of Sakamoto and Nakatsuka [18] for Zircaloy-2, together with literature data for Zr-2.5%Nb alloy [19,20]. Two calculations were made using Eq. (4), with stress effect coefficients of F = 2 and 3. A crack initiated from the outer surface of the tube propagated almost linearly with time, and the average calculated DHC rates in the temperature range of 200–275 °C were half that of Sakamoto and Nakatsuka. On the other hand, the activation energy of the calculated DHC rates is 38 kJ/mol, in good accordance with the value (36 kJ/mol) of the experiments. Of properties used in the model that affect the DHC rate, two have temperature dependences - the diffusion coefficient of hydrogen (activation energy: 35 kJ/mol) and the yield stress of Zircaloy-2. In order to resolve the difference between the experimental and calculated DHC rates, more sophisticated fracture mechanics model may be needed.
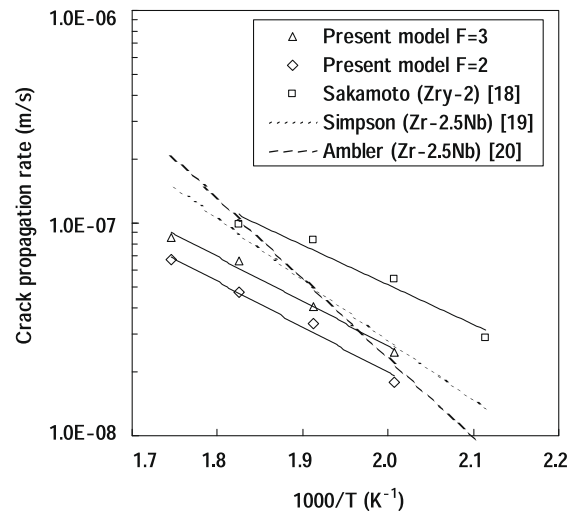

Fig. 13. Comparison of calculated DHC propagation rates with experimental data using Zircaloy-2 and Zr-2.5%Nb alloy.
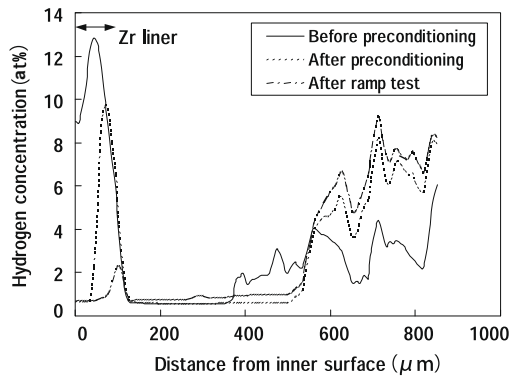
Fig. 14. Calculated hydrogen distributions in the Zircaloy-2 cladding with Zr liner before and after preconditioning at 200 W/cm for 15 h, and after ramp test at 428 W/cm for 1 h.

4.2.4. Thermal diffusion of hydrogen in power ramp condition

Outside-in type cracking in high burnup BWR fuels arising in power ramp tests is attributed to hydride embrittlement in the outermost region of the cladding [1]. One possible explanation is that, during power transients, hydrogen that had accumulated in the region of the Zr liner diffused toward tube's cooler outside region, resulting in radial hydride growth under the stress orientation mechanism.

To simulate an actual power ramp test [1], a model calculation was conducted using the following conditions: BWR fuel rod of 8 × 8 size (0.86 mm cladding thickness, 0.09 mm Zr liner thickness); initial average hydrogen content of 3 at.% (335 ppm); a preconditioning power level of 200 W/cm for 15 h; terminal power at ramp test of 428 W/cm; circumferential stress at ramp test of 300 MPa. Unfortunately, since the present model cannot reproduce exactly an initial distribution of hydride in the cladding, a similar distribution was made by trial and error. Calculated hydrogen distributions in the cladding before and after the preconditioning and after the ramp test of 1.0 h are shown in Fig. 14. In the initial condition, hydrogen of about 10 at.% is heterogeneously accumulated in Zr liner region. After the preconditioning of 200 W/cm for 15 h, more than the half of the accumulated hydrogen is thermally diffused toward the outer region of the cladding, and at the ramp condition of 428 W/cm the remaining hydrogen in Zr liner disappears during 1 h. The calculated hydrogen distribution after the power ramp is roughly consistent with the reported result [1]. Newly formed radial hydrides in the outside region driven by thermal diffusion are assumed to be linked with crack initiation and propagation.

5. Conclusions

The terminal solid solubility of hydrogen during the dissolution of hydrides (TSSD) at heat up and during the precipitation of hydrogen at cool down were measured for Zircaloy-2 cladding tubes and spacer bands irradiated in commercial BWRs, using DSC technique. Fast neutron fluence ($E > 1$ MeV) and hydrogen concentration of the specimens were 5.4–12.9 × 10^{25} n/m² and 21–373 ppm. The data of archived unirradiated specimens were also obtained for a comparison. In the DSC response of as-irradiated specimens during the first heating stage, exothermic reactions resulting from the recovery of irradiation defects added to the

original endothermic reactions of hydride dissolution above irradiation temperature of 288 °C. In the case of the post-irradiation annealed specimens, the recovery became remarkable above the annealing temperatures. While this competing reaction made the DSC peak of hydride dissolution dull or broader, no significant difference was detected in the TSS between unirradiated and irradiated Zircaloy-2, irrespective of neutron fluence. The results suggest almost no interaction between irradiation defects and dissolved hydrogen or hydrides at temperatures around 300 °C. Finally, best-fit equations for the TSSD and TSSP solvi of irradiated, as well as unirradiated Zircaloy-2 were given by

$$C_{TSSD} \text{ (ppm)} = 1.43 \times 10^5 \exp(-36,686/RT),$$

$$C_{TSSP} \text{ (ppm)} = 3.27 \times 10^4 \exp(-25,042/RT),$$

where R is the gas constant (8.314 J K^{-1} mol^{-1}) and T is the temperature in K.

Using the present TSS data and reported hydrogen- and hydride-related properties, a microscopic analysis code HYMAC for analyzing hydrogen and hydride behavior was constructed; the latter has a two dimensional diffusion space of circumferential and radial directions of cladding tube with textured grains. Stress-induced preferential precipitation and dissolution of hydrides were reproduced by adopting a TSS sub-model in which the solubilities decrease in proportion to stress normal to the habit plane in grains and to grain faces. Analyzed results by the model were consistent with typical experimental results of hydride-related behavior, such as stress reorientation of hydride, thermal diffusion of hydrogen, and delayed hydride cracking (DHC).

References

[1] S. Shimada, Y. Etoh, H. Hayashi, Y. Tsukuda, J. Nucl. Mater. 327 (2004) 97.
[2] A. McMinn, E.C. Darby, J.S. Schofield, Zirconium in the nuclear industry, in: Twelfth International Symposium, ASTM STP 1354, 2000, p. 173.
[3] P. Vizcaino, A.D. Banchik, J.P. Abriata, J. Nucl. Mater. 304 (2002) 96.
[4] H.M. Cheng, R.S. Daum, J.M. Hiller, M.C. Billone, Zirconium in the Nuclear Industry, in: Thirteenth International Symposium, ASTM STP 1423, 2002, p. 561.
[5] K. Ogata, T. Baba, K. Kamimura, T. Kubo, K. Une, Y. Etoh, Paper Presented at Fifteenth International Symposium on Zirconium in the Nuclear Industry, Sunriver, USA, June 24–28, 2007.
[6] K. Une, S. Ishimoto, J. Nucl. Mater. 322 (2003) 66.
[7] K. Une, S. Ishimoto, J. Nucl. Sci. Technol. 41 (9) (2004) 949.
[8] M. Amaya, K. Une, K. Minato, J. Nucl. Mater. 294 (2001) 1.
[9] J.J. Kearns, J. Nucl. Mater. 22 (1967) 292.
[10] P. Vizcaino, A.D. Banchik, J.P. Abriata, J. Nucl. Mater. 336 (2005) 4.
[11] K. Une, K. Nogita, S. Ishimoto, K. Ogata, J. Nucl. Sci. Technol. 41 (7) (2004) 731.
[12] K. Une, S. Ishimoto, J. Nucl. Mater. 357 (2006) 147.
[13] B.F. Kammenzind, B.M. Berquist, R. Bajaj, P.H. Kreyns, D.G. Franklin, Zirconium in the nuclear industry, in: Proceedings of the Twelfth International Symposium, ASTM STP 1354, 2000, p. 196.
[14] M.P. Puls, Metall. Trans. A21 (1990) 2905.
[15] H.M. Chung, in: Proceedings of 2004 International Meeting on LWR Fuel Performance, Orland, Florida, September 19–22, 2004, Paper 1064.
[16] M. Aomi, K. Kamimura, T. Baba, T. Miyashita, in: International Conference on Management of Spent Fuel from Nuclear Power Reactors, June 19–22, 2006, Vienna, Austria.
[17] K. Sakamoto, N. Nakatsuka, J. Nucl. Sci. Technol. 43 (9) (2006) 1136.
[18] K. Sakamoto, N. Nakatsuka, in: Proceedings of 2008 Water Reactor Fuel Performance Meeting, Seoul, Korea, October 19–23, 2008, Paper 8009.
[19] L.A. Simpson, M.P. Puls, Met. Trans. A10 (1979) 1093.
[20] J.F.R. Ambler, Zirconium in the nuclear industry, in: Sixth International Symposium, ASTM STP 824, 1984, p. 635.
[21] S. Sawatzky, J. Nucl. Mater. 2 (1960) 62.
[22] S. Sawatzky, J. Nucl. Mater. 2 (1960) 321.
[23] M.P. Puls, Acta Metall. 32 (1984) 1259.
[24] Y. Mishima, T. Okubo, M. Oishi, T. Aoki, Nippon Genshiryoku Gakkai-shi 29 (2) (1987) 90 (in Japanese).